

Two-Dimensional and Three-Dimensional Time-Lapse Microscopic Magnetic Resonance Imaging of *Xenopus* Gastrulation Movements Using Intrinsic Tissue-Specific Contrast

Cyrus Papan,^{*†} Benoit Boulat, S. Sendhil Velan,[‡] Scott E. Fraser, and Russell E. Jacobs

The amphibian embryo undergoes radical tissue transformations during blastula and gastrula stages, but live observation of internal morphogenetic events by optical microscopy is not feasible due to the opacity of the early embryo. Here, we report on the use of microscopic magnetic resonance imaging (MRI) to directly follow morphogenetic movements during blastula and gastrula stages of the *Xenopus laevis* embryo. We compare three different MRI modalities that take advantage of the intrinsic contrast present in embryonic tissues: three-dimensional (3D) fat-imaging, 3D water-imaging, and 2D high-speed high-resolution imaging of early embryonic stages. We show that the features revealed by the intrinsic contrast correlate with the histological structure of the embryo. Using this tissue specific intrinsic contrast, the main embryonic tissues and internal tissue movements as well as archenteron invagination can be differentiated without cell labeling. We present 2D and 3D time-lapse sequences of early *Xenopus* embryonic development, spanning the stages from early blastula to the end of gastrula, which show the complex internal rearrangements of gastrulation in essentially real-time. *Developmental Dynamics* 236:494–501, 2007.

© 2006 Wiley-Liss, Inc.

Key words: *Xenopus laevis*; gastrula; MRI; longitudinal study; 3D imaging; morphogenesis

Accepted 14 November 2006

INTRODUCTION

Understanding developmental mechanisms operating in the *Xenopus* embryo has often been hampered by inaccessibility of the live embryo to optical microscopy, due to light scattering by the intracellular yolk inclusions. Experiments on morphogenetic movements and their molecular control have relied on tissue explants or the interpretation of movements from static histological

preparations (Vogt, 1929; Brachet, 1935; Nieuwkoop and Florschütz, 1950; Keller, 1975, 1976; Nakatsuji, 1975; Bauer et al., 1994; Winklbauer and Schürfeld, 1999; Davidson et al., 2002; Davidson and Keller, 2004). However, early cleavages are irregular, and it has been found that even the most prominent gastrulation features like archenteron inflation, invagination, and blastopore closure do not occur at in-

variant times in relation to each other (Ewald et al., 2004). Such properties make the reconstruction of amphibian gastrulation movements from time-course data problematic, thus highlighting the necessity for time-lapse studies in the same embryo.

Magnetic resonance imaging (MRI) has several advantages over other imaging modalities, which makes it ideally suited for live imaging of

The Supplementary Material referred to in this article can be viewed at <http://www.interscience.wiley.com/jpages/1058-8388/suppmat>

Beckman Institute, California Institute of Technology, Pasadena, California

Grant sponsor: NCCR-BIRN, Grant number: NIH RR13642; Grant sponsor: Deutsche Forschungsgemeinschaft; Grant number: PA 562/1-1.

[†]Dr. Papan's present address is Institute of Bioengineering and Nanotechnology, 31 Biopolis Way, The Nanos 04-01, Singapore 138669.

[‡]Dr. Velan's present address is West Virginia University, Department of Radiology and Center for Advanced Imaging, One Medical Center Drive, HSC South, PO Box 9236, Morgantown, WV 26506-9236.

*Correspondence to: Cyrus Papan, Institute of Bioengineering and Nanotechnology, 31 Biopolis Way, The Nanos 04-01, Singapore 138669. E-mail: cpapan@ibn.a-star.edu.sg

DOI 10.1002/dvdy.21045

Published online 26 December 2006 in Wiley InterScience (www.interscience.wiley.com).

gastrulation in the optically opaque amphibian. It does not depend on optical properties of tissues and can non-invasively (Kay et al., 1988) visualize internal structures in opaque biological tissue (Lauterbur, 1973; Redpath, 1997). It is able to acquire whole three-dimensional (3D) images of embryos. Even with most modern optical methods, such as confocal microscopy or optical coherence tomography (Haskell et al., 2004), it is a very difficult, if not impossible, task to acquire complete 3D-images of whole live embryos. However, the acquisition of 3D images is of crucial importance for quantitative studies of embryonic morphogenesis, which happens in three dimensions. Furthermore, MRI is able to differentiate biological tissue based on tissue-specific intrinsic magnetic properties (Johnson et al., 1993), a property that has made magnetic resonance imaging an invaluable tool for medical diagnostics.

Previously conducted MRI of frog embryos made use of extrinsic contrast to follow tissue movements during blastula and gastrula stages (Jacobs and Fraser, 1994) and intrinsic tissue contrast for tracing cell lineages of early blastomeres (Papan et al., 2006). Here, we show that intrinsic tissue contrast in the MR images correlates with the histological structure of the early embryo and can be used for studying tissue morphogenesis during blastula and gastrula stages. We compare three different MRI modalities, each highlighting the morphology of the embryo in a different way and allowing us to distinguish the main embryonic tissue regions and boundaries, such as the animal cap, the marginal zone, the vegetal cell mass, the Cleft of Brachet, the blastocoel, and the archenteron. 2D and 3D time-lapse sequences are presented that show morphogenetic tissue movements of gastrulation and archenteron invagination.

RESULTS AND DISCUSSION

Intrinsic Tissue Contrast of Water and Fat Images of *Xenopus* Embryos

Magnetic resonance images of the amphibian embryo can be generated sep-

arately from the various nuclear magnetic resonance (NMR) signals present in the *Xenopus* embryo. This is because tissue water and the lipids exhibit separate proton-NMR frequencies: 4.7 ppm for the tissue water and multiple resonances between 0.5 and 6 ppm for the methine-, methyl-, and methylene groups of the lipids (Sehy et al., 2001). Hence, images formed from the NMR signal of the tissue water are designated “water images,” and images formed from the NMR signal of the tissue lipids are designated “fat images.”

Figure 1 shows a comparison of tissue contrast in water and fat images. In water images (Fig. 1A–D), the blastocoel(bc) displays the highest signal intensity, the animal cap tissue (ac) has an intermediate, and vegetal cell mass (veg) the lowest intensity. The fluid surrounding the embryo is also dark because Feridex has been added to the Rearing medium to suppress its NMR signal (see the Experimental Procedures section). Fat images (Fig. 1I–L) show the opposite contrast to water images, with the strongest signal intensity at the vegetal pole (veg), lower intensity in the animal cap (ac), and no signal in the blastocoel (bc). Due to the much lower total concentration of fat protons compared with water protons, the signal-to-noise (S/N) ratio is lower than in water images. However, because fat is present only in the tissue, image contrast is high. Thus, water and fat images present two imaging modalities, which highlight the animal cap and the vegetal cell mass in a complementary manner.

The reason for this tissue contrast is the higher yolk content at the vegetal pole (Danilchik and Gerhart, 1987; Hausen and Riebesell, 1991), which results in differential T1, T2, and spin density values in the different embryonic regions (Sehy et al., 2001). It should be noted that, to suppress the fat signal in the water images, we used an initial 90 degrees selective radio frequency (RF) pulse centered around 1.2 ppm with a subsequent dephasing gradient. Although most of the lipid resonances are located at 1.2 ppm, we cannot exclude a residual contribution to the “water images” of some lipid signal located around 5.2 ppm, close to the water resonance.

Correlation of MRI Contrast With Histology

To correlate MRI contrast with the tissue architecture, we compared water (Fig. 1A–D) and fat (Fig. 1I–L) images to histological images (Fig. 1E–H) of embryos of comparable developmental stage. Figure 1E shows the familiar histological structure of the blastula stage *Xenopus* embryo (Hausen and Riebesell, 1991), with the smaller less yolky cells of the animal cap, the larger more yolky cells of the vegetal pole, and cells of intermediate size in the marginal zone. This structure correlates well with the contrast seen in the corresponding MR images (Fig. 1A,I): The animal cap is bright and the vegetal pole is dark, and the boundary between the light and the dark moiety (indicated with white dashed lines) coincides with the boundary between the small and the large cells. At stage 10 (Fig. 1F), the embryo is asymmetric because the dorsal marginal zone (DMZ) is populated with small cells, while the ventral marginal zone (VMZ) is not (see also panel 18 in Hausen and Riebesell, 1991). This asymmetry is also seen in the MRI images (Fig. 1B,J). At stage 11 (Fig. 1G), the mesendodermal mantle is moving over the inside of the animal cap toward the animal pole and is separated from the animal cap tissue by the Cleft of Brachet (Brachet, 1935, arrow in Figure 1G). In the MR images, it is visible as a sharp interface between the darker tissue of the vegetal cell mass and the brighter regions of the animal cap (Fig. 1G, arrow). At stage 12 (Fig. 1H), the archenteron (ar) has formed and is clearly visible in the MR image. Between the blastocoel and the archenteron, there is a region of loosely arranged cells with large intercellular spaces. This region is discernible in the MR images as well (asterisk in Fig. 1). The thickening of the anterior neuroectoderm (an), evident in the histological images (Fig. 1H), is also visible in the water MR image (Fig. 1D).

Thus, tissue contrast in the MR images of early *Xenopus* embryos correlates well with the characteristic difference in cell size between the animal cap and the vegetal cell mass, a result of the higher yolk concentration toward the vegetal pole in the amphibian-

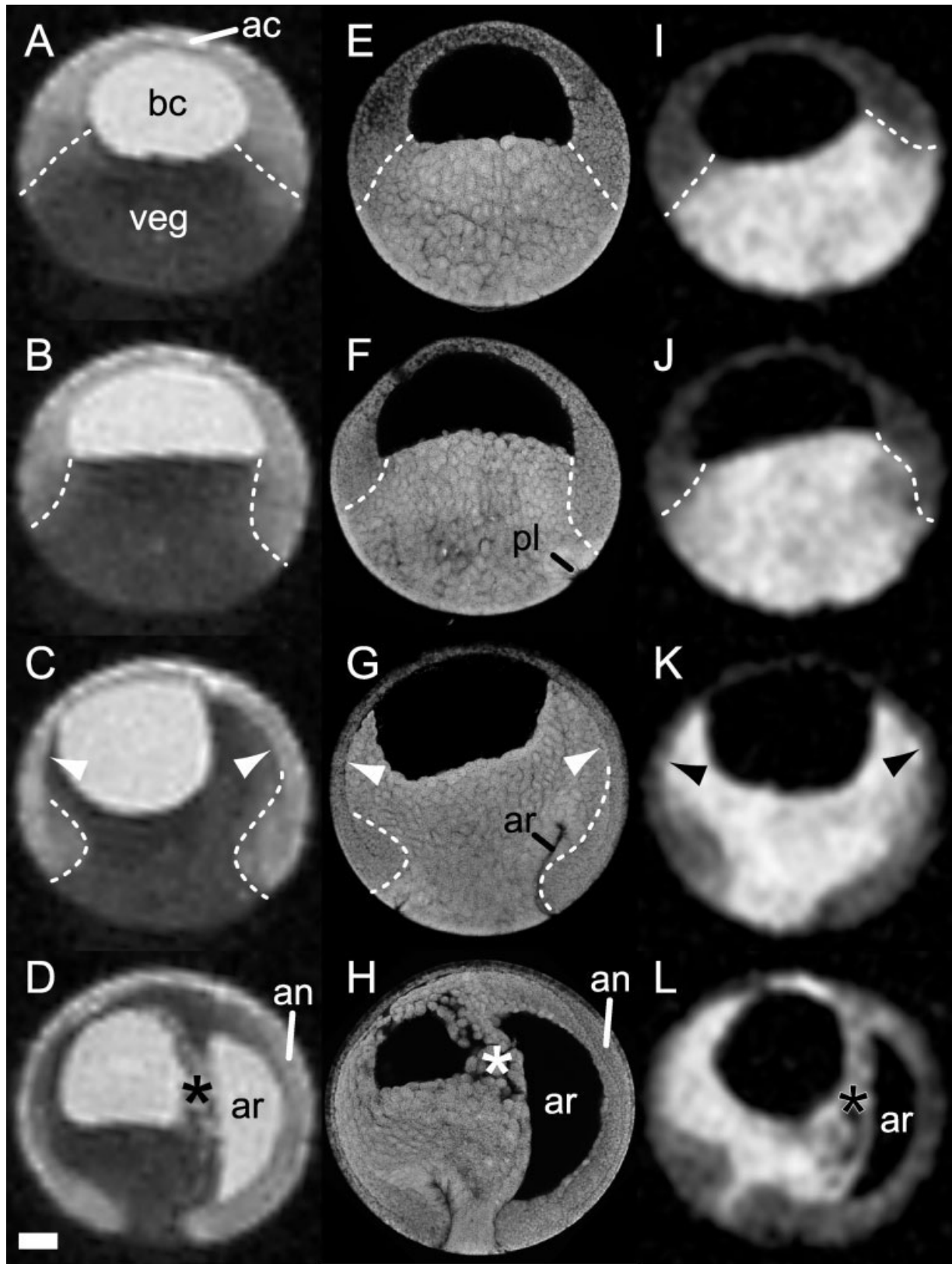


Fig. 1. A–L: Time-lapse series of water (A–D) and fat (I–L) magnetic resonance (MR) images in comparison with a time course series of histological images (E–H) at comparable embryonic stages. A,E,I, stage 9; B,F,J, stage 10; C,G,K, stage 11; D,H,L, stage 12. All images are sagittal, the animal pole is up, and dorsal is to the right. Dashed lines in the MR images (A, B, C, and I, J) demarcate the intensity boundary between the vegetal and the animal cells, which corresponds to the boundary between smaller animal and larger vegetal cells in the confocal images, also indicated with a dashed line in the histological images (E, F, and G). ac, animal cap; veg, vegetal cell mass; bc, blastocoel; pl, pigment line; ar, archenteron; an, anterior neuroectoderm (see text); asterisks, regions of loosely packed cells (see text); arrowheads, Cleft of Brachet. Scale bar = 200 μ m.

ian mesolecithal eggs (Danilchik and Gerhart, 1987). The intrinsic contrast seen in the early embryo is similar to what has been observed in *Xenopus* oocytes (Sehy et al., 2001). Although not strictly lineage specific, the contrast can be used as a specific marker for tracing morphogenetic movements of different tissue regions through gastrulation.

3D Time-Lapse Visualization of *Xenopus* Gastrulation From Water Images

To visualize the internal morphogenetic changes of the embryo structure through blastula and gastrula, we carried out 3D surface renderings of a time series of MR water image volumes. Figure 2 shows selected stages from such a series. At stage 8 (Fig. 2A), the embryo is rotational symmetric, with the animal cap at the top and the vegetal cell mass at the bottom. From stage 8 (Fig. 2A) to stage 9 (Fig. 2B), the embryo changes little except for the enlargement of the blastocoel. By stage 10 (Fig. 2C), the blastocoel has further enlarged and the embryo is no longer symmetric, because the DMZ (black arrow in Fig. 2C) is larger than the VMZ (black arrowhead in Fig. 2C). The entire blastocoel floor (BCF) has lifted up, and is higher on the dorsal side (white arrow in Fig. 2C) compared with the ventral side (white arrowhead in Fig. 2C). By stage 11 (Fig. 2D), the mesendodermal mantle has assumed its characteristic cup shape, and the dorsal rim (black arrow in Fig. 2D) is further advanced than the ventral rim (black arrowhead in Fig. 2D). The red animal cap tissue has advanced toward the vegetal pole. By stage 12, the archenteron (green sphere in Fig. 2E) has begun to inflate on the dorsal side, and the blastocoel assumes its characteristic funnel-shape with the funnel tip pointing toward the archenteron (asterisk in E). By stage 12.5, the archenteron has inflated further, pushing the blastocoel ventrally. The animal cap has almost completely enclosed the vegetal cell mass except for the yolk plug (yp).

With the acquisition parameters used here, we were able to acquire a 3D image in less than 1 hr at a resolution of $39 \mu\text{m}^3$. By keeping the embryo at 15°C , the spatial and temporal

resolution was sufficient to follow morphogenetic movements during gastrulation, which at this temperature takes ~ 12 hr. Increasing the S/N ratio or image resolution through pulse sequence manipulations, however, inevitably results in a lengthening of the imaging time. Fixed biological samples may be scanned for extended periods to reach a desired S/N ratio, but imaging live samples is restricted by morphogenetic or body movements. Our image acquisition parameters were consequently determined by acquisition time constraints.

3D Time-Lapse Visualization of Vegetal Cell Mass Morphogenesis From Fat Images

The high signal intensity of the vegetal pole seen in fat images allows a selective 3D surface rendering of the vegetal cell mass (VCM) from fat-image volumes. Figure 3 shows a time-lapse sequence from mid-blastula to the end of gastrula, illustrating the morphogenetic changes in the VCM. At stage 9 (Fig. 3A), the VCM is radial-symmetric, the BCF is concave, and the edge (indicated with a dashed black line in Fig. 3) is irregular. Around stage 9.5 (Fig. 3B), the BCF has expanded and its edge has become more regular. Around stage 10 (Fig. 3C), the BCF has further expanded and has become convex. On the dorsal side, the leading edge of gastrulation has begun to move upward (white arrow in Fig. 3C). At stage 10.25 (Fig. 3D), the advancement of the leading edge has also started on the ventral side (white arrowhead in Fig. 3D). At stage 10.5 (Fig. 3E), the VCM has assumed a cup shape, as the leading edge has circumferentially begun to move toward the animal pole. At stage 12 (Fig. 3F), the leading edge is about to fuse at the animal pole (white arrow), with the mesendodermal mantle nearly enclosing the blastocoel. In the lateral wall of the mesendodermal mantle, a hole can be seen (black arrow in Fig. 3F), corresponding to a region of lower intensity. Such a region was not observed in other 3D fat images. It most likely represents a susceptibility artifact due to a nearby particle, which are in some cases

found stuck to the vitelline membrane of a dejellied embryo.

It should be noted that the contrast between the animal and the vegetal region is not sharply defined. Thus, when segmenting the images for surface rendering either in water images or in fat images, a change in the threshold chosen for rendering may change the result significantly. However, keeping the threshold constant between time points allows the direct comparison and measurement of morphological changes within a given time series.

2D High-Resolution, High-Speed Imaging

At gastrula, the *Xenopus* embryo is bilateral-symmetric, so that for many purposes 2D imaging of the sagittal plane (the midline) contains sufficient information about the embryo structure. The higher image resolution and signal-to-noise (S/N) ratio at shorter imaging times offset the disadvantage of losing the 3D information. Figure 4 (see also Supplementary Movie S3 and Movie S4, which can be viewed at <http://www.interscience.wiley.com/jpages/1058-8388/suppmat>) shows selected stages of a 2D time sequence. Strikingly, marginal zone tissue can be differentiated from animal cap (AC) tissue and the VCM, and its morphogenetic movement can be traced through the gastrula stages.

At stage 10 (Fig. 4A), the marginal zone tissue is located in the equatorial region between the AC tissue and the VCM. The dorsal blastoporal lip is visible (black arrows in Fig. 4A,B), which was not apparent in a 3D image (Fig. 1). At stage 11 (Fig. 4B), gastrulation movements have changed the structure of the embryo. Both the dorsal and the ventral equatorial regions now consist of three distinct layers, with the black VCM on the inside, an orange layer on the outside and the dark red marginal zone tissue in between (indicated by light blue arrows in Fig. 4B). The interface between the outer and the middle layer corresponds to the Cleft of Brachet (black arrowheads in Fig. 4B,C). At stage 12 (Fig. 4C) the archenteron (ar) has formed, separating the black vegetal cell mass and the archenteron roof. The archenteron roof is composed of two distinct layers: the light orange ectoder-

mal layer and the dark orange/red mesodermal layer. The boundary between both layers corresponds to the Cleft of Brachet, which was not as evident in the 3D images of the comparable stage (Fig. 1D). Other morphological features are visible as well: The mesendodermal mantle has just closed (black arrow in C). The yolk plug (yp) is still present. Just as in the 3D water image (Fig. 1D), the anterior neuroectoderm (an) is visible as a thickening of the outer layer of the archenteron roof.

In conclusion, though sacrificing the 3D information, 2D imaging acquires images faster and at a much higher S/N ratio than 3D imaging, thus allowing a better differentiation of the embryonic tissues and boundaries. Although not strictly lineage-specific, the intrinsic contrast gives a clear impression of the tissue movements of the marginal zone during gastrula. The chosen slice thickness of 200 μm captured a sufficiently large region of the embryo while exhibiting a good feature resolution with the main features of interest being visible. Slice thicknesses of 400 μm or 500 μm resulted in too much loss of resolution due to partial volume artifacts. Multiple slice 2D imaging is an obvious extension that can be done without lengthening the total imaging time.

Time-Lapse Imaging of Archenteron Invagination

One of the main hallmarks of gastrulation is the formation of the archenteron. While its initial formation could not be revealed in 3D MR images, the early phases of this process can directly be followed in 2D time-lapse sequences. Figure 5 shows a time sequence illustrating this early invagination phase (see also the Supplementary Movie S4). The tip of the archenteron can be discerned as a bright spot penetrating into the darker tissue of the vegetal cell mass. At 0:00, approximately stage 10.5, the archenteron has just begun to invaginate. In the following time points, the process of invagination can be followed as the tip of the archenteron (white arrows in Fig. 5) moves animal-ward. At 1:45, the archenteron has reached a length of approximately 400 μm . The time series shows that its extent is not en-

tirely a result of actual invagination. This is because the archenteron is also extending toward the posterior due to the epibolic movement of the animal cap. At time 1:45 (Fig. 4), the current location of the blastopore is indicated in relation to the original

position (indicated by an arrowhead). Thus, approximately 150 μm of the archenteron's length at this time point is due to epiboly, while approximately 250 μm is due to invagination. This finding is an example for the requirement of a longitudinal study by

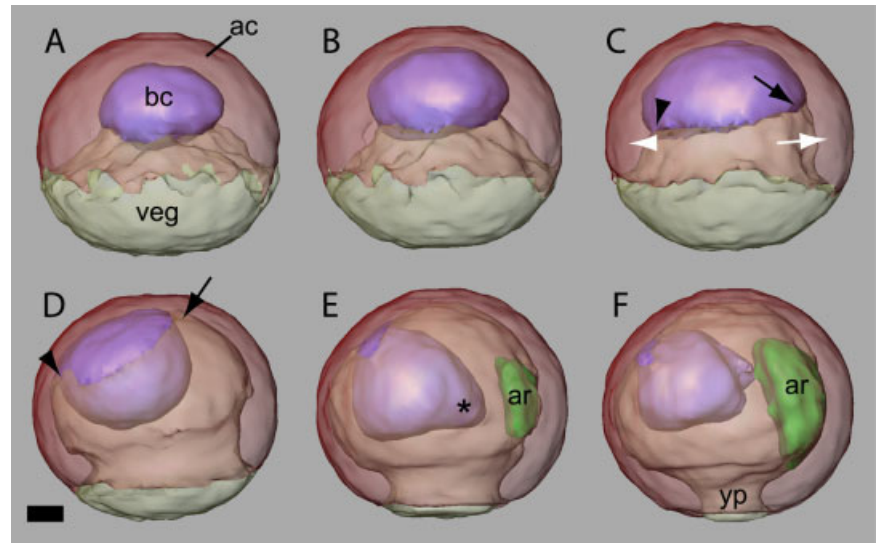


Fig. 2.

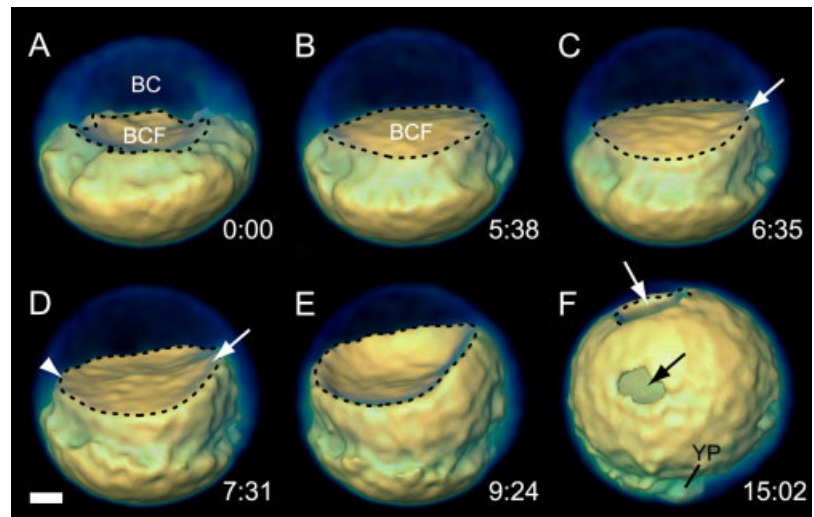


Fig. 3.

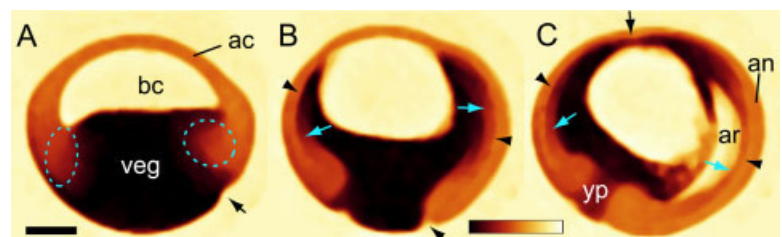


Fig. 4.

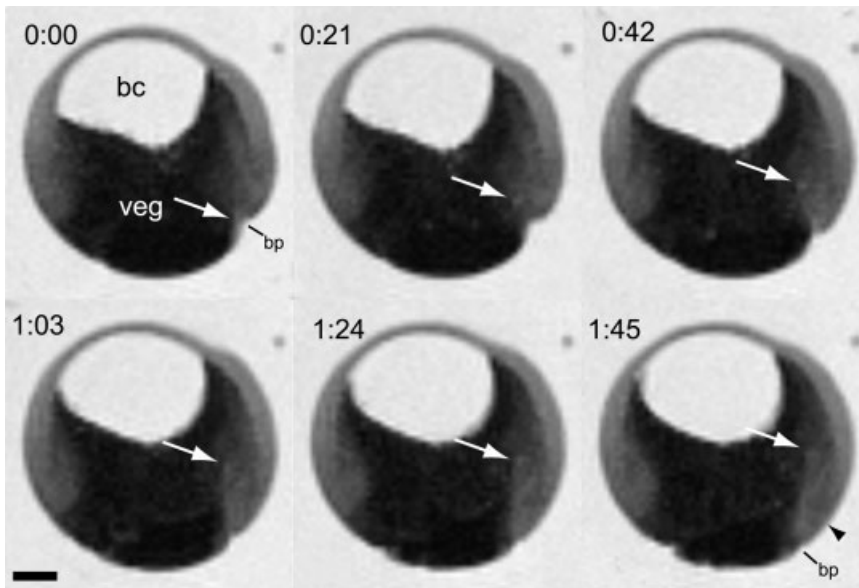


Fig. 5. Two-dimensional (2D) time-lapse series illustrating the early phase of archenteron invagination. Times are indicated in hr:min with relation to the first scan. Images are sagittal, and embryos are oriented with the animal pole up and dorsal is to the right. Bc, blastocoel; veg, vegetal cell mass. The tip of the archenteron is visible as a small brighter dot (white arrows), traveling from the blastoporal lip (bp) animal-ward. The arrowhead at 1:45 points at the original location of the blastoporal lip. Scale bar = 200 μ m.

MRI, as the extension of the archenteron cannot be traced from time course data due to the weak correlation

between external staging criteria (blastopore closure) and internal morphogenesis (Ewald et al., 2004).

Fig. 2. A–F: Three-dimensional (3D) surface-rendered time series of an embryo showing internal morphogenetic changes during *Xenopus* blastula and gastrula stages. A, stage 8; B, stage 9; C, stage 10; D, stage 11; E, stage 12; F, stage 12.5. The embryo is oriented with dorsal to the right and the animal pole up. The vegetal cell mass (veg) is rendered yellow, the animal cap (ac) red, the blastocoel (bc) blue, and the archenteron (ar) green. The animal cap and the vegetal cell mass are transparent to facilitate visualization of internal structures. Black arrowhead, ventral leading edge of the mesendodermal mantle; black arrow, dorsal leading edge of the mesendodermal mantle; white arrowhead, ventral marginal zone; white arrow, dorsal marginal zone; asterisk, tip of the blastocoel pointing toward the archenteron; yp, yolk plug. Scale bar = 200 μ m.

Fig. 3. A–F: Three-dimensional (3D) time series of an embryo showing the morphogenetic transformations of the vegetal cell mass during blastula and gastrula stages. The vegetal cell mass is surface rendered in yellow, and the remainder of the embryo is volume rendered in blue/green to provide the context of the whole embryo. Embryos are shown in a lateral view with the dorsal side to the right and a slight tilt toward the animal pole to facilitate the view on to the blastocoel floor. A, stage 8; B, stage 9.5; C, stage 10; D, stage 10.25; E, stage 10.5; F, stage 12. Scan times are indicated in hr:min with respect to the first scan. bc, blastocoel; BCF, blastocoel floor. Dashed lines indicate the edge of the BCF. White arrows in C and D, dorsal leading edge of the mesendodermal mantle. White arrowhead in D, ventral leading edge of the mesendodermal mantle. White arrow in F, site where the mesendodermal mantle will eventually close. Black arrow in F, hole in the lateral wall of the mesendodermal mantle; yp, yolk plug. Scale bar = 200 μ m.

Fig. 4. A–C: Selected images from a two-dimensional (2D) high-resolution high-speed time lapse series showing the morphogenetic movements of the dorsal and ventral marginal zone. The animal pole is up, dorsal to the right. Slices are sagittal. A, stage 10; B, stage 11; C, stage 12. ac, animal cap; bc, blastocoel; veg, vegetal cell mass; an, thickening of the anterior neuroectoderm; yp, yolk plug. Images have been median filtered, and a color look-up table (shown at the bottom of the panel) has been applied, rendering the animal cap in orange, the marginal zone in dark orange/red, and the vegetal cell mass in black. In A, the dark orange/red marginal zone tissue is encircled with a dashed line. In B and C, the light blue arrows indicate the dark orange/red tissue underlying the light orange animal cap tissue. Black arrowheads, Cleft of Brachet. Black arrows in A and B, dorsal blastoporal lip. Black arrow in C, point of closure of the mesendodermal mantle. Scale bar = 300 μ m.

CONCLUSIONS AND OUTLOOK

In this study, we describe the use of intrinsic MRI tissue contrast for time-lapse imaging of *Xenopus* gastrulation. The main advantage of a live imaging technique to study gastrulation is that it avoids the variability of the same developmental processes between different embryos. This variability makes reconstruction of dynamic morphogenetic processes from time course data difficult and potentially unreliable. *Xenopus* is known to vary considerably in key aspects of morphogenesis: Early cleavages are highly variable and rarely “textbook like,” requiring the careful selection of embryos exhibiting such standardized cleavage patterns. In addition, a pronounced divergence between internal and external morphogenetic characteristics has recently been described (Ewald et al., 2004) but was previously unrecognized.

Various applications for the described imaging method in studying *Xenopus* gastrulation can be envisioned. With the ability to record 3D data sets, MRI opens up the possibility of a precise quantification of the morphogenetic transformation of gastrulation. Numerous morphogenetic parameters can be extracted, for example, the timing and speed of mesendodermal mantle advancement, archenteron invagination, animal cap epiboly, and asymmetry between the dorsal and the ventral marginal zone. The surface areas and the volumetric data of tissues or subregions of tissues can be obtained from semiautomatic image segmentation and may be easily measured with existing software. In this way, MRI can provide a quantitative link between tissue morphogenesis and the results of molecular perturbations used to test hypotheses about the underlying mechanisms.

With the different contrast sources available, various aspects of the development can be imaged. While water imaging is useful for tracing the animal cap epiboly, formation of the embryonic cavities and archenteron invagination, fat imaging can be used for imaging the vegetal pole of the embryo. Fat imaging is particularly useful for experiments that require labeling of cells in the VCM. Although a

T1-contrast agent has successfully been used to label cells at the animal pole (Jacobs and Fraser, 1994), such agents do not markedly enhance contrast of vegetal cells (C. Papan, unpublished observations). This is likely due to the lower free-water content in this region. However, we found that cells in the VCM could be successfully labeled with a commercially available suspension of superparamagnetic iron oxide (SPIO) nanoparticles (Feridex, Berlex), which reduces the signal in the labeled cells, thus allowing to trace cells in the VCM (C. Papan, unpublished observations).

With a view to the application of MRI to the study of gastrulation in nonamphibian species, it is important to consider that the main contrast source in the amphibian is the asymmetric distribution of the yolk. The yolk-containing blastomeres participate in the formation of the embryo, which is not the case in teleosts or avian embryos. Additionally, gastrulation of those embryos occurs in a comparatively thin cell layer on the outside of a large yolk cell. With a 2D image resolution of 23 μm^2 , the cell layer would thus only be covered by approximately 5–6 pixels. In addition, avian embryos are contained within a large egg, which requires the usage of a much larger RF coil and larger field of view.

In its present state, the imaging technique shown is best suited for monitoring relatively large morphogenetic changes of the embryo. To visualize cell movements in more detail, cell labeling will be required. However, it is expected that future hardware developments might make it possible to directly visualize cells in the later blastula and gastrula without cell labeling. A contrast agent may be applied nonspecifically to the entire embryo, shortening the T1-value of the tissue and thus allowing for a higher S/N ratio in the same imaging time (M. Tyszka, personal communication). Microsurface coils (Bilgen, 2004) could be used to visualize the embryo at much higher resolution than currently attainable, or the use of a recently available cryoprobe (Lee et al., 2005) may also improve the S/N ratio.

Although MRI is an expensive technique, and its successful implemen-

tation requires specially trained personnel, it is becoming more and more common, especially in the rapidly expanding field of mouse models for human diseases (Ahrens et al., 1998; Benveniste and Blackband, 2002) and in the neuroscience of small primates like mouse lemurs (Dhenain et al., 1997, 2000). All of these disciplines require MRI instrumentation similar to that used in this work, which are now more commonly available in shared imaging facilities of many research facilities and universities. This availability puts microscopic MRI well within the reach of labs not specialized in this imaging technique.

EXPERIMENTAL PROCEDURES

Embryo Handling and Mounting

Embryos were derived by *in vitro* fertilization (Sive et al., 1998) and kept in Rearing medium (0.8% Instant Ocean, Aquarium Systems, Mentor, OH) throughout. Embryo staging was done according to Nieuwkoop and Faber (1994). For 3D experiments, the jelly coat of the embryos was removed at the four- to eight-cell stage by incubating them in 2% cysteine pH 8.0 for 4–5 min. For imaging purposes, embryos were placed in a D₂O susceptibility-matched glass tube (BMS-0025, Shigemi Corp., Tokyo, Japan; outer diameter 2.5 mm, inner diameter 1.9 mm) in approximately 10 μl of Rearing medium. Both ends of the tube were sealed with a Teflon membrane (High Sensitivity Membrane Kit, YSI Inc., Yellow Springs, OH) to allow oxygen exchange while preventing water evaporation. For 3D spin-echo MR experiments, the Rearing medium was supplemented with Feridex (Berlex) at 1:40 dilution to suppress its MR signal, thus making the image data better suitable for 3D volume renderings. Development of embryos in the glass tubes was indistinguishable from control sibling embryos developing in a Petri dish until at least stage 24, when the surrounding drop size becomes too small to accommodate the extending embryo. To slow down the development, the MR scanning was done at 15°C. At this temperature, gastrulation takes approximately 12

hr, yielding sufficient temporal resolution to follow development. For reliable embryonic axis identification in 2D experiments, the early blastula stage embryos were oriented with the aid of the asymmetric pigmentation (Masho, 1990; Sive et al., 1998), either perpendicular or parallel to the long axis of the sample tube. For optical imaging, embryos were fixed in Bouin's fixative for 2 hr at room temperature. Fixed embryos were bisected with a razor blade along the body midline to facilitate better imaging of the embryos sagittal plane, then dehydrated in a graded ethanol series and cleared and mounted in benzyl benzoate/benzyl alcohol (2:1 v/v) in depression slides. Confocal imaging was done using a Zeiss LSM 510 Axiovert or a Zeiss LSM 5 Pascal Axiovert microscope with a C-Apochromat 10X/0.45 W objective and the pinhole set to 2 airy units, using the 488-nm laser line to excite the tissue autofluorescence.

Image Acquisition

MR images were acquired using a Bruker Avance DRX500 spectrometer (11.7 T) with microimaging capability (Bruker BioSpin Corp, Billerica, MA). A home-built 3-mm solenoidal RF coil (Papan et al., 2006) wrapped around a hollow glass tube into which the sample tube was inserted was used for all data collection. For 3D imaging, we used a T1-weighted spin-echo pulse sequence with TR/TE = 400 msec/8 msec and two averages yielding an imaging time of 55 min. The field of view was typically 5 × 2.5 × 2.5 mm with an array size of 128 × 64 × 64, resulting in approximately 39 μm^3 isotropic voxel size. For fat suppression in the water images, a fat-selective RF pulse centered at 1.2 ppm followed by a dephasing gradient pulse was used at the beginning of the sequence. To suppress water in the fat images, we used an initial water-selective 90 degrees RF pulse followed by a dephasing gradient; then performed a fat-selective 90 degrees RF pulse. For 2D imaging, we used a gradient echo imaging with repetition time TR/TE = 400 msec/5.7 msec and eight averages, yielding an imaging time of 6 min and 44 sec. Slice thickness was 200 μm ; the field of view was typically 3 × 3 mm with an array size

of 128×128 , resulting in approximately $23 \mu\text{m}^2$ in-plane resolution.

ACKNOWLEDGMENTS

We thank Andrey Demyanenko for coil development and Mike J. Tyszka, Seth Ruffins, and Rachel S. Kraut for critical discussions and suggestions.

REFERENCES

- Ahrens ET, Laidlaw DH, Readhead C, Brosnan CF, Fraser SE, Jacobs RE. 1998. MR microscopy of transgenic mice that spontaneously acquire experimental allergic encephalomyelitis. *Magn Reson Med* 40:119–132.
- Bauer DV, Huang S, Moody SA. 1994. The cleavage stage origin of Spemann's Organizer: analysis of the movements of blastomere clones before and during gastrulation in *Xenopus*. *Development* 120:1179–1189.
- Benveniste H, Blackband S. 2002. MR microscopy and high resolution small animal MRI: applications in neuroscience research. *Prog Neurobiol* 67:393–420.
- Bilgen M. 2004. Simple, low-cost multipurpose RF coil for MR microscopy at 9.4 T. *Magn Reson Med* 52:937–940.
- Brachet A. 1935. *Traité d'Embryologie des Vertébrés*. Paris: Masson et cie.
- Danilchik MV, Gerhart JC. 1987. Differentiation of the animal-vegetal axis in *Xenopus laevis* oocytes. I. Polarized intracellular translocation of platelets establishes the yolk gradient. *Dev Biol* 122:101–112.
- Davidson LA, Hoffstrom BG, Keller R, DeSimone DW. 2002. Mesendoderm extension and mantle closure in *Xenopus laevis* gastrulation: combined roles for integrin $\alpha(5)\beta(1)$, fibronectin, and tissue geometry. *Dev Biol* 242:109–129.
- Dhenain M, Michot JL, Volk A, Picq JL, Boller F. 1997. T2-weighted MRI studies of mouse lemurs: a primate model of brain aging. *Neurobiol Aging* 18:517–521.
- Dhenain M, Michot JL, Privat N, Picq JL, Boller F, Duyckaerts C, Volk A. 2000. MRI description of cerebral atrophy in mouse lemur primates. *Neurobiol Aging* 21:81–88.
- Ewald AJ, Peyrot SM, Tyszka JM, Fraser SE, Wallingford JB. 2004. Regional requirements for Dishevelled signaling during *Xenopus* gastrulation: separable effects on blastopore closure, mesendoderm internalization and archenteron formation. *Development* 131:6195–6209.
- Haskell RC, Williams ME, Petersen DC, Hoeling BM, Schile AJ, Pennington JD, Seetin MG, Castelaz JM, Fraser SE, Papan C, Ren H, de Boer JF, Chen Z. 2004. Visualizing early frog development with motion-sensitive 3-D optical coherence microscopy. In: Annual International Conference of the IEEE EMBS. San Francisco, CA.
- Hausen P, Riebesell M. 1991. The early development of *Xenopus laevis*. Berlin: Springer-Verlag.
- Jacobs RE, Fraser SE. 1994. Magnetic resonance microscopy of embryonic cell lineages and movements. *Science* 263:681–684.
- Johnson GA, Benveniste H, Black RD, Hedlund LW, Maronpot RR, Smith BR. 1993. Histology by magnetic resonance microscopy. *Magn Reson Q* 9:1–30.
- Kay HH, Herfkens RJ, Kay BK. 1988. Effect of magnetic resonance imaging on *Xenopus laevis* embryogenesis. *Magn Reson Imaging* 6:501–506.
- Keller RE. 1975. Vital dye mapping of the gastrula and neurula of *Xenopus laevis*. I. Prospective areas and morphogenetic movements of the superficial layer. *Dev Biol* 42:222–241.
- Keller RE. 1976. Vital dye mapping of the gastrula and neurula of *Xenopus laevis*. II. Prospective areas and morphogenetic movements of the deep layer. *Dev Biol* 51:118–137.
- Keller R, Davidson L. 2004. Cell movements of gastrulation. In: Stern CD, editor. *Gastrulation: from cells to embryo*. Cold Spring Harbor, NY: Cold Spring Harbor Laboratory Press.
- Lauterbur PC. 1973. Image formation by induced local interactions: examples employing nuclear magnetic resonance. *Nature* 242:190–191.
- Lee HL, Lin IT, Horng HE, Yang HC. 2005. High-T_c superconducting receiving coils for nuclear magnetic resonance imaging. *IEEE Trans Appl Superconductivity* 15:1326–1329.
- Masho R. 1990. Close correlation between the 1st cleavage plane and the body axis in early *Xenopus* embryos. *Dev Growth Differ* 32:57–64.
- Nakatsuji N. 1975. Studies of the gastrulation of amphibian embryos: cell movement during gastrulation in *Xenopus laevis* embryos. *Roux Arch Dev Biol* 178:1–14.
- Nieuwkoop PD, Faber J. 1994. Normal table of *Xenopus laevis* (Daudin): a systematic and chronological survey of the development from the fertilized egg till the end of metamorphosis. New York, London: Garland Publishing, Inc. 252 p.
- Nieuwkoop PD, Florschütz PA. 1950. Quelques caracteres speciaux de la gastrulation et de la neurulation de l'oeuf de *Xenopus laevis* Daud. et de quelques autres anoures. *Arch Biol* 61:113–150.
- Papan C, Boulat B, Velan SS, Fraser SE, Jacobs RE. 2006. Time-lapse tracing of mitotic cell divisions in the early *Xenopus* embryo using microscopic MRI. *Dev Dyn* 235:3059–3062.
- Redpath TW. 1997. MRI developments in perspective. *Br J Radiol* 70 Spec No:S70–S80.
- Sehy JV, Ackerman JJ, Neil JJ. 2001. Water and lipid MRI of the *Xenopus* oocyte. *Magn Reson Med* 46:900–906.
- Sive HL, Grainger RM, Harland RM. 1998. Early development of *Xenopus laevis*: a laboratory manual. Cold Spring Harbor, NY: Cold Spring Harbor Laboratory Press.
- Vogt W. 1929. Gestaltungsanalyse am Amphibienkeim mit örtlicher Vitalfärbung. *W Roux Arch f Entw Mech Org* 120.
- Winklbauer R, Schürfeld M. 1999. Vegetal rotation, a new gastrulation movement involved in the internalization of the mesoderm and endoderm in *Xenopus*. *Development* 126:3703–3713.